Proceedings of IMECE'01
2001 ASME International Mechanical Engineering Congress and Exposition
November 11-16, 2001, New York, NY, USA

PIRANI PRESSURE SENSOR WITH DISTRIBUTED TEMPERATURE SENSING

J.J. van Baar
MESA+ Research Institute
University of Twente
P.O. Box 217, 7500 AE Enschede
The Netherlands
E-mail: J.vanBaar@el.utwente.nl

Coauthors
R.J. Wiegerink
T.S.J. Lammerink
G.J.M. Krijnen
and M. Elwenspoek

ABSTRACT

A Pirani pressure sensor is based on the fact that the thermal conductivity of a gas is dependent on the pressure. The structure presented in this paper consists of a heated microbeam, which is placed above a v-groove in a heat sink. The temperature distribution along the microbeam is a measure for the thermal conductivity of the surrounding gas. Measuring the temperature distribution instead of the average temperature of the beam has two advantages: the measurement becomes independent of the Temperature Coefficient of Resistance of the temperature sensing resistors and the heat loss to the substrate is implicitly taken in account, which extends the lower pressure range.

INTRODUCTION

In the molecular range the thermal conductivity of a gas is proportional to the pressure as found by M. von Pirani in 1906 (vP06). This fact can be exploited in Pirani pressure sensors, where a heat source and heat sink are placed at close distance from each other. The distance has to be smaller than the mean free path of the gas molecules.

An important advantage of Pirani sensors is their robustness. They do not contain any moving parts (e.g. a bending membrane) and are not damaged when an overpressure is applied. A disadvantage is that the output signal also depends on the type of gas.

Various implementations of Pirani sensors can be found in the literature, e.g. using different heater shapes like cantilevers (vHS87), microbridges (BK94) or plates, using a v-groove cavity (WS94) or thin sacrificial layer (Pau95) to realize the narrow gap between heater and heat sink, having heat transfer lateral (SN94) or perpendicular to the wafer surface, using $< 100 >$ or $< 111 >$ (CCS99) wafers and using two bonded wafers (AJB95).

The sensor presented in this paper consists of a heated microbridge, which is placed above a v-groove in the substrate. The difference with existing sensors is that the temperature distribution is measured instead of the average temperature of the microbeam. The shape of this temperature distribution depends on the pressure, which makes the absolute temperature rise unimportant. This has the advantage that the measurement becomes independent of the Temperature Coefficient of Resistance of the temperature sensing resistors.

Figure 1 shows a schematic drawing of the structure. A platinum heater is placed along the center of a thin silicon nitride carrier. Additional platinum leads are connected to the heater, dividing it into five segments. The voltage drop across each of these segments can be measured individually. The temperature dependent electrical resistance can be calculated from the voltage drop and the current through the heater. The average temperature of each segment is calculated from the change in electrical resistance of the segment. A discretized model for fitting the average temperatures of the five segments is used to extract the pressure.

THEORY

The pressure dependence of the thermal conductivity can be split up in three regions: molecular, viscous slip and viscous, see figure 2. From microscopic considerations of kinetic theory the thermal conductivity κ $[W/Km]$ can be derived for an ideal,

Copyright © 2001 by ASME

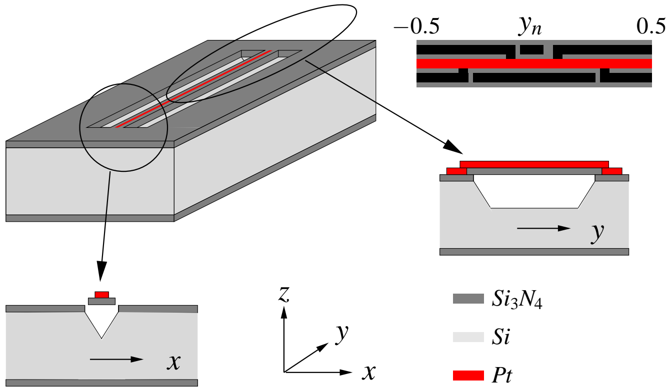

Figure 1. Schematic drawing of the structure

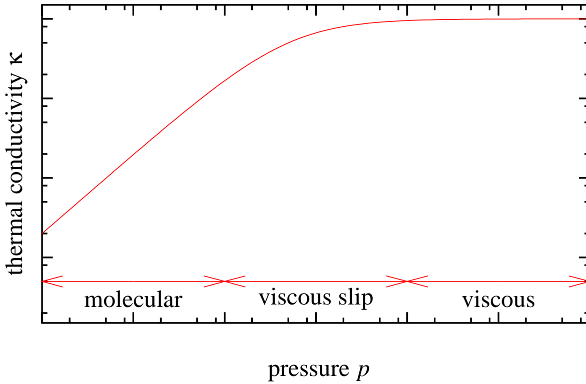

Figure 2. Thermal conductivity as function of pressure (loglog-plot)

dilute gas in (Rei65)

$$\kappa = \frac{1}{3}\, n\, \bar{v}\, c\, \lambda \tag{1}$$

with c the pressure independent specific heat per molecule and $\bar{v}$ the mean molecular velocity. In the viscous region κ is pressure independent, because the number of particles in a volume, n, and the mean free path λ of the molecules are directly and inversely proportional to the gas pressure, respectively. In the molecular range the thermal conductivity is proportional to the number of molecules, because the mean-free-path is limited by the characteristic length of the system.

The thermal conductance G_g measured between the heater and heat sink in a Pirani sensor depends on the pressure in the same way as the thermal conductivity. This dependence can be described by the following equation (vS11):

$$G_g = A_s K P \left(\frac{P_t}{P + P_t}\right) \tag{2}$$

with the constant K depending on the type of gas and the accommodation coefficient, the pressure P_t depending on the characteristic length of the system, i.e. the distance between heater and heat sink and A_s is the effective surface area of the sensor..

MODEL

The temperature profile $T(\mathbf{y_n})$ along the length of the beam is dependent on the ratio between heat transport through the gas and through the beam. It can be calculated using the following second order differential equation (Bru94).

$$-\frac{1}{R'_b}\frac{\partial^2 T(\mathbf{y_n})}{\partial y_n^2} + G'_f T(\mathbf{y_n}) = \mathbf{P'} \tag{3}$$

where $\mathbf{y_n}$ is the normalized position along the beam and $\mathbf{P'}$ is the electrical line power in $[W/m]$. The temperature profile is dependent on the thermal line resistance of the beam R'_b $[K/(Wm)]$, the thermal line conductance through the gas G'_f $[W/(Km)]$ and the length of the beam l $[m]$.

The solution of equation 3 is given by (Bru94)

$$\Delta T(\mathbf{y_n}) = \frac{P'}{G'_f}\left(1 - \frac{\cosh\left(y_n \cdot l\sqrt{R'_b G'_f}\right)}{\cosh\left(\frac{1}{2}\, l\sqrt{R'_b G'_f}\right)}\right) \tag{4}$$

Normalizing the temperature distribution of equation 4 to the temperature rise at the center of the beam results in:

$$T_n(\mathbf{y_n}) = \frac{\Delta T(\mathbf{y_n})}{\Delta T(0)} = \frac{\cosh\left(\frac{1}{2}\, l\sqrt{R'_b G'_f}\right) - \cosh\left(y_n \cdot l\sqrt{R'_b G'_f}\right)}{\cosh\left(\frac{1}{2}\, l\sqrt{R'_b G'_f}\right) - 1} \tag{5}$$

Figure 3 shows a plot of this normalized temperature distribution for several values of the term $l\sqrt{R'_b G'_f}$ ranging from 0 to 20. The advantage of normalizing in this manner is the cancelling out of the Temperature Coefficient of Resistance, which is otherwise needed to know the temperature.

In a practical sensor the temperature cannot be measured in a single point. Instead the average temperature over a segment is measured. Integration of equation 4 and dividing by the length of the segment results in the following expression for the average segment temperature per unit applied line power $[W/(Km)]$ for a segment with lower boundary a and upper boundary b, which both are normalized to l:

Copyright © 2001 by ASME

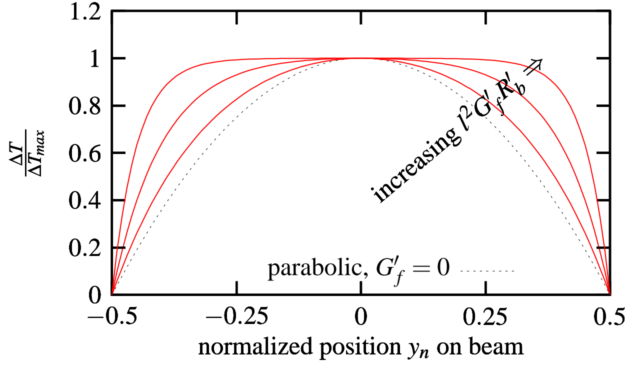

Figure 3. Normalized temperature distribution along the beam

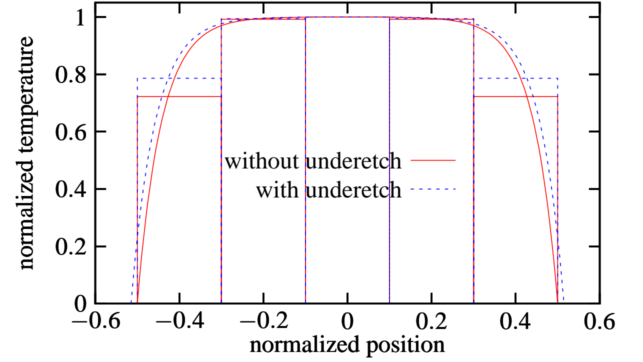

Figure 4. Average of the normalized temperature of the segments and the normalized temperature distribution versus the normalized position along all segments with and without underetch.

$$\frac{\bar{T}(a,b)}{P'} = \frac{1}{G'_f}\left(1 - \frac{\sinh\left(b\,l\sqrt{R'_b G'_f}\right) - \sinh\left(a\,l\sqrt{R'_b G'_f}\right)}{(b-a)\,l\sqrt{R'_b G'_f}\,\cosh\left(\frac{1}{2}\,l\sqrt{R'_b G'_f}\right)}\right) \quad (6)$$

Averaging the normalized temperature distribution of equation 5 over the length of the resistor segment gives:

$$\bar{T}_n(a,b) = \frac{\cosh\left(\frac{1}{2}\,l\sqrt{R'_b G'_f}\right)}{\cosh\left(\frac{1}{2}\,l\sqrt{R'_b G'_f}\right) - 1} - \frac{\sinh\left(b\,l\sqrt{R'_b G'_f}\right) - \sinh\left(a\,l\sqrt{R'_b G'_f}\right)}{(b-a)\,l\sqrt{R'_b G'_f}\,(\cosh\left(\frac{1}{2}\,l\sqrt{R'_b G'_f}\right) - 1)} \quad (7)$$

Figure 4 shows a plot of the normalized temperature distribution (equation 5) together with the average temperature per segment indicated by boxes (equation 7). Due to underetch the beam length l will be somewhat larger than designed. The dashed curve in figure 4 illustrates the influence of this underetch. Equation 7 is used for interpretation of the measurement results using a realistic value for l including the underetch.

A rough estimate for the line conductance G'_f in equations 3 to 7 can be obtained using a parallel plate approximation, as indicated in figure 5. $G'_f = \kappa\, w/d_{eff}$ with the width w $[m]$ and the effective depth d_{eff} $[m]$. Using an effective depth equal to half of the groove depth d $[m]$ gives a value for G'_f around $3.3 \cdot 10^{-2}$ $W/(Km)$ in the case the thermal conductivity of the fluid is $26 \cdot 10^{-3}$ $W/(Km)$, the depth 41 μm and the width of the beam 25 μm. The underetching of the support has been drawn.

A better estimate for the line conductance G'_f can be obtained using the lumped element model shown in figure 6. In this model only the heat transfer in the direction perpendicular to the beam is considered: no heat transfer through the beam to its edges is assumed. The light gray elements respresent the thermal conductances in horizontal direction and the dark gray elements represent the conductances in vertical direction. For each node in the lumped element model Kirchhoffs current law can be applied (VS83) resulting in the thermal conductance matrix **G**. Inverting

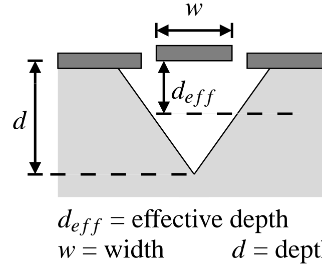

Figure 5. Cross section of the v-groove, with underetched support, which has an effective depth d_{eff} taken half of the depth of the groove.

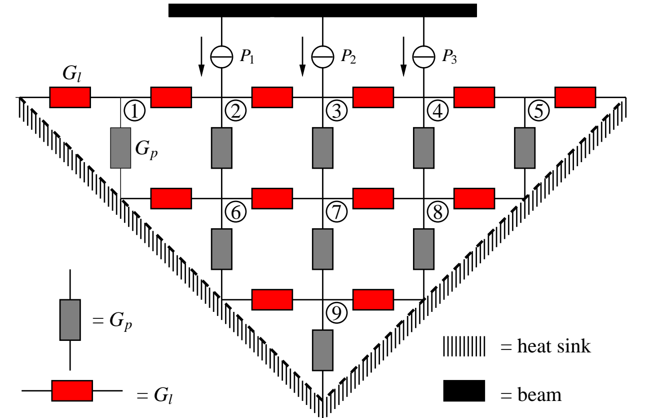

Figure 6. Lumped element model with nine nodes drawn

Copyright © 2001 by ASME

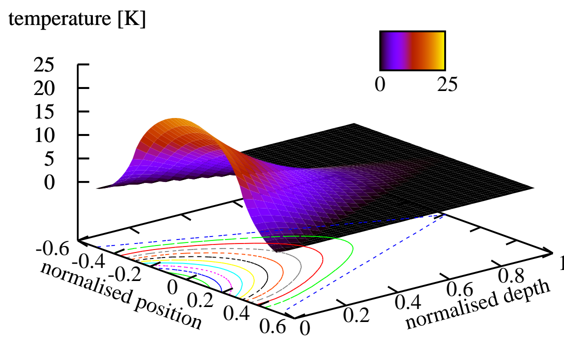

Figure 7. 2D Temperature distribution of the v-groove

this matrix and multiplying it with the power **P** gives the temperature distribution **T** in the v-groove under the beam.

The sum of the ratios between the applied power P_i and the temperature difference T_j between the beam and the heat sink gives the value of the effective thermal conductance G'_f, with in the case of figure 6 i=1,2,3 and j=2,3,4. This gives a value around $5 \cdot 10^{-2}\ W/(Km)$ in the case the width of the v-groove is 60 μm. This value is somewhat larger than the previously calculated value using the very rough parallel plate approximation. Figure 7 shows a plot of the calculated temperature distribution in the v-groove.

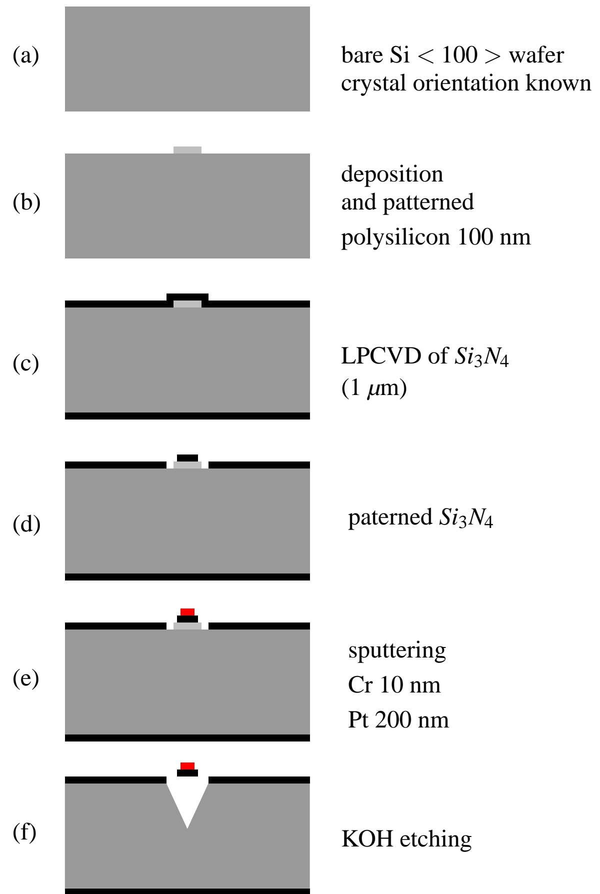

Figure 8. Process steps

REALIZATION

Figure 8 shows the process sequence used for fabrication of the sensor chips. The first step of the process is the deposition of a 1 μm thick Si_3N_4 layer on a silicon (100) wafer, with a thickness of approximately 380 μm. A special mask structure is used in combination with KOH-etching for precisely finding the crystallographic orientation (VB96). This step is necessary because of the large length to width ratio of the v-groove. A slight misalignment results in a large underetch, which widens the v-groove.

The next steps are selectively stripping of the Si_3N_4 and the deposition of a 100 nm thick sacrificial polysilicon layer. The latter is needed for underetching of the beam. After patterning the poly-Si layer a Si_3N_4 layer is deposited and patterned. A 10 nm chromium primary layer and a 200 nm platinum layer are sputtered and after lift-off, KOH etching is used for releasing the beam. The KOH etching would normally stop at a depth of about 21 μm. However, due to a very long etching time (required for some other structures on the same chip, see (vBWL+01)) a significant underetch occurs, resulting in a v-groove with a depth of about 41 μm.

Figure 9 shows a photograph of the first two segments of a beam (with a total of five segments). The underetch is clearly visible. The beam itself has a length of 1 mm, a width of 25 μm and thickness of 1 μm. The platinum heater and voltage leads have a width of 5 μm and a thickness of 200 nm.

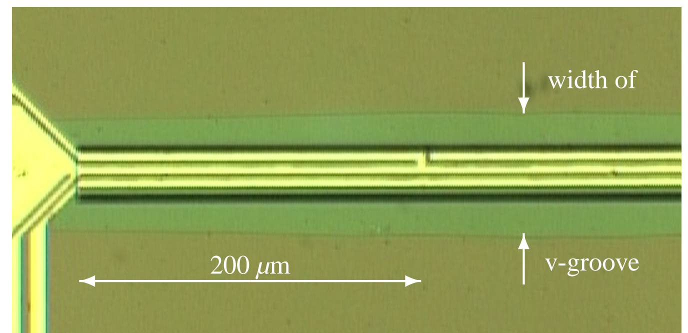

Figure 9. Photograph of part of the beam with heater divided in five segments

Copyright © 2001 by ASME

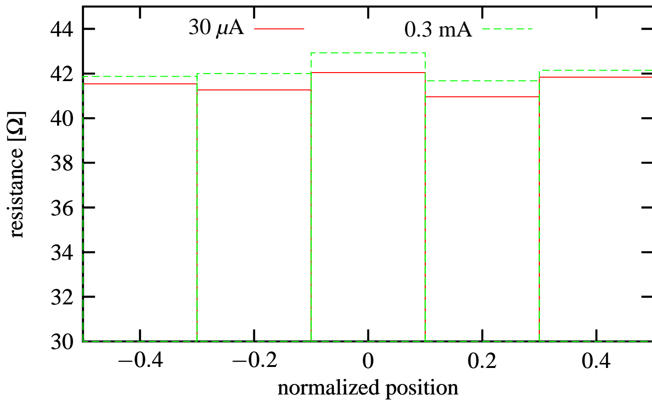

Figure 10. Resistances of the segments for currents of 30 μA and 0.3 mA at 3.5 Pa.

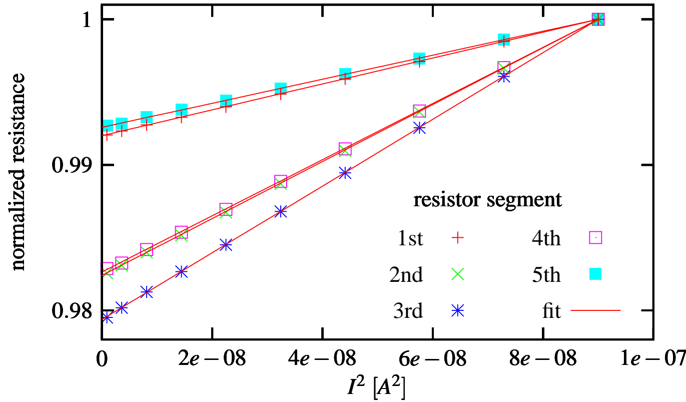

Figure 11. Resistances of the segments normalized to the resistance at 0.3 mA for currents from 30 μA to 0.3 mA. The fit is lineair and gives us the extrapolated resistance at I=0 A. The temperature rise is proportional to the applied power.

MEASUREMENTS

As mentioned before, the voltage drop across each segment can be measured individually. To measure the resistance of a segment a current is applied to the heater and the resulting voltage drop is measured, corresponding to a four point measurement. Figure 10 shows a plot of the resistance values for two different heating currents, 30 μA and 0.3 mA. The spread in resistance values is due to random variations of the platinum line-width due to the lift-off process. The dependence on the applied current is due to the resulting change in temperature. The relative change in resistance is a measure for the temperature. We see that this change is largest for the center segment, which has the highest temperature.

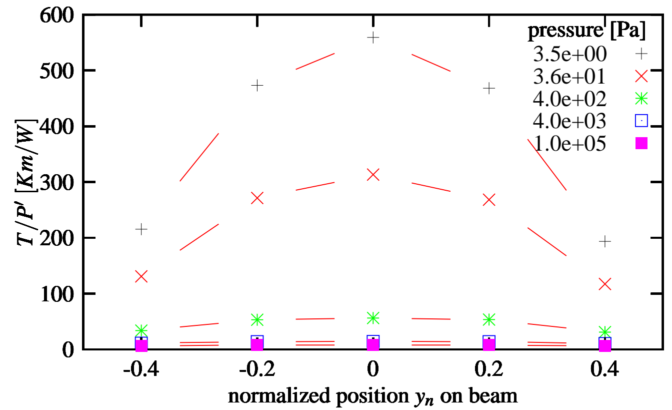

Figure 12. Measured temperature per unit line power versus the normalized position on the beam for several pressures

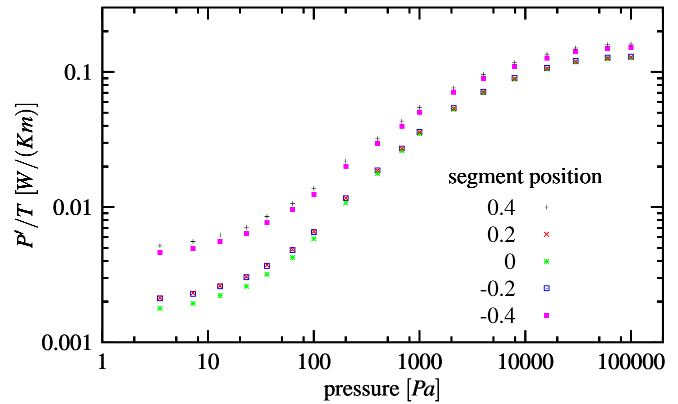

Figure 13. Line power per unit temperature versus pressure for each resistor segment. The lowest curve is from the center segment.

To obtain the temperature of a segment we first need to know the resistance when there is no heating current applied. This is done by measuring the resistance at several current levels as shown in figure 11. The resistance is linearly dependent on the temperature and, therefore, on the heating power. All curves are normalized to the value at a current of 0.3 mA. Extrapolation of the curves results in the resistance value at zero heating current.

Measurements have been performed using nitrogen with the pressure ranging from 3.5 Pa up to atmospheric pressure. For the different pressures care is taken to keep the maximum temperature rise between 5 and 10 K. To eliminate the variation of the required applied power the temperature distribution along the beam has been divided by the line power, see figure 12. Measurements from the same data set are plotted in a different way in figure 13. The ratio of line power and temperature rise is plotted as a func-

Copyright © 2001 by ASME

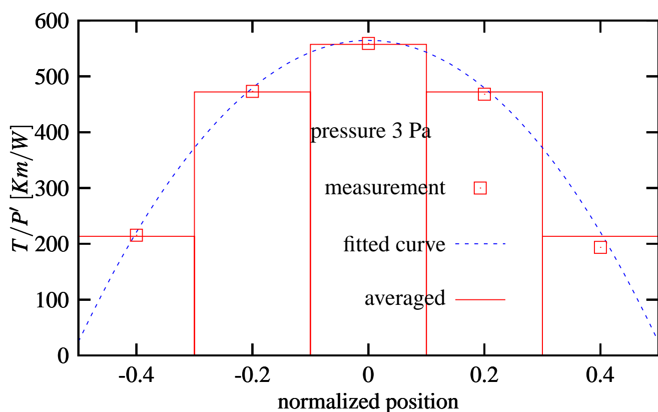

Figure 14. Temperature distribution per unit line power versus the normalized position at 3.5 Pa.

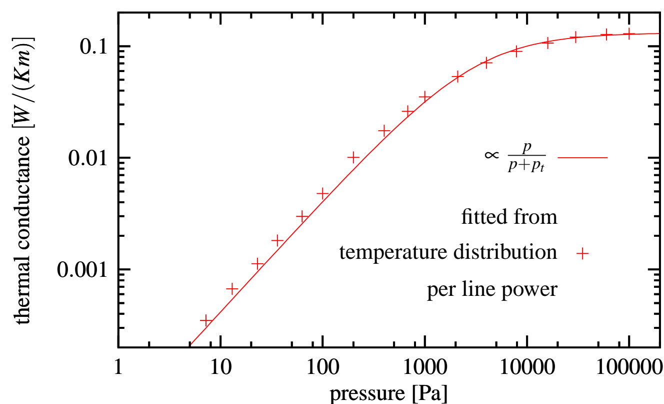

Figure 16. Thermal conductance versus pressure obtained from the temperature distribution per line power for the fluid nitrogen.

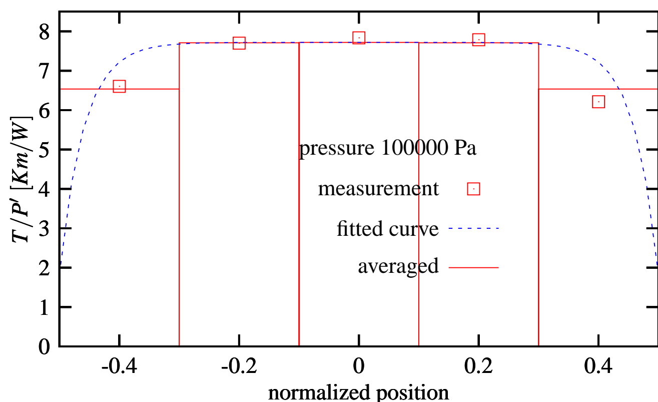

Figure 15. Temperature distribution per unit line power versus the normalized position at 1 bar.

tion of pressure for each segment. The bottom curve corresponds to the center segment and the top curves correspond to the outer segments of the beam. The two upper curves are not identical as would be expected. This is due to the fact that a cap was placed over the chip, which was needed for other structures on the same chip. Misalignment of this cap causes a slightly asymmetrical temperature profile. We see that for low pressures the sensitivity decreases because the heat transfer through the beam dominates the heat transfer through the gas.

Figures 14 and 15 show the measured temperature distribution of figure 12 for 3.5 Pa and $1 \cdot 10^5$ Pa, respectively. These measurements are fitted using function 6, which gives the thermal conductance. The dashed curve is the temperature distribution predicted by the model. The average temperature over each segment (indicated by the boxes) is fitted to the measurement data. An implementation of the nonlinear least-squares Marquardt-Levenberg algorithm has been used. For the thermal resistance of the beam a value of $R_b = 4.7e+9K/(Wm)$ was taken for all pressures. Theoretically this value should be $4e+8K/(Wm)$, however the difference corresponds very well to earlier results with flow sensors (vBWL$^+$01). Using equation 6 results in the fitted thermal conductances of figure 16. The transition pressure P_t is $2.5 \cdot 10^3$ Pa.

For the thermal conductance to the fluid at atmosperic pressure $0.128K/(Wm)$ was found. The theoretical value obtained from the rough lumped element model was $5 \cdot 10^{-2}$. The deviation can be explained by the fact that several factors have been neglected. In the model the heat transfer through the beam (for a homogeneous temperature), the Si_3N_4 flaps due to underetch, the thermal conductance to the cap and free convection were not taken in account.

An effective enlargement of the beam due to underetch is taken 20.5 μm, while the underetch was 40 μm. In this effective enlargement can be taken in account that the width of the support is much larger than the width of the beam, which will result in a lower thermal line resistance.

The normalized temperature distribution is the measured temperature distribution divided by the temperature rise in the center. Measurements from the same data set as used in figure 12 can be applied to obtain figure 17. In this figure it can be seen clearly that the shape changes with the pressure. The normalized temperature has been fitted with equation 7 for several pressures, see figures 18 and 19. The product $R'_b G'_f$ has been fitted and the thermal conductivity of the fluid has been normalized to the value at atmospheric pressure, see figure 20.

Note that for the temperature distribution per line power the R_b and G_f are fitted and for the temperature distribution normalized to the temperature rise of the center segment only the

Copyright © 2001 by ASME

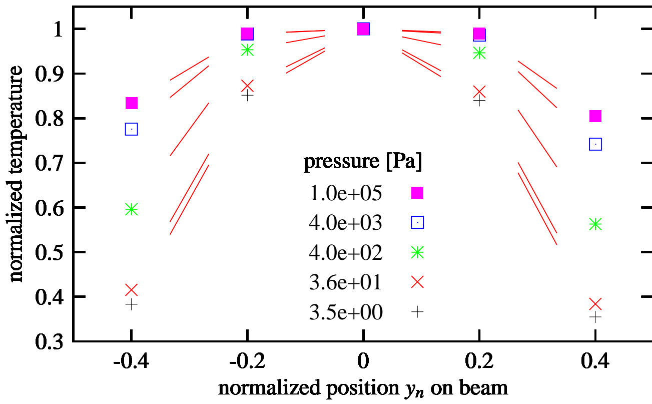

Figure 17. Measured temperature distribution normalized to the temperature rise of the center segment versus the normalized position on the beam for several pressures.

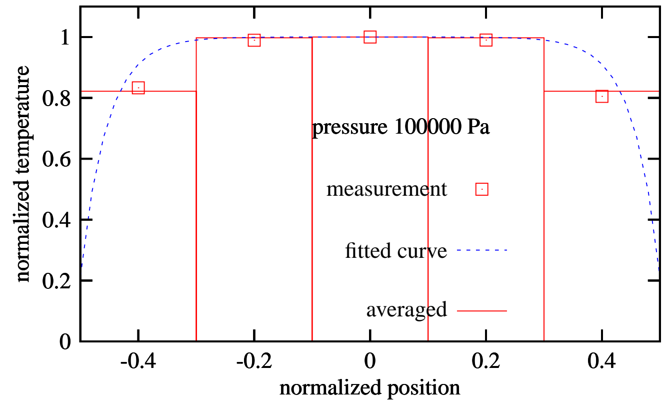

Figure 19. Temperature distribution normalized to the temperature rise of the center segment versus the normalized position at 1 bar with fit

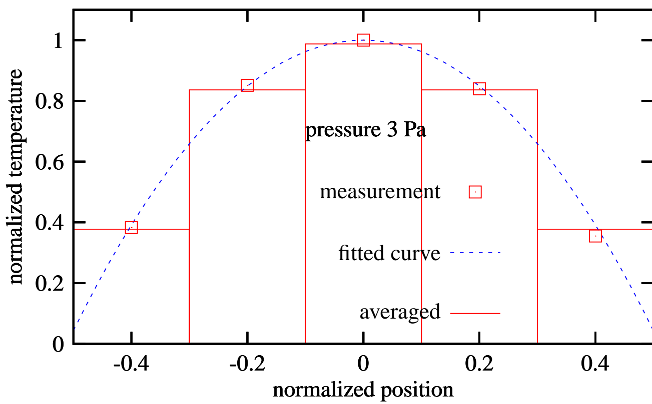

Figure 18. Temperature distribution normalized to the temperature rise of the center segment versus the normalized position at 3.5 Pa with fit

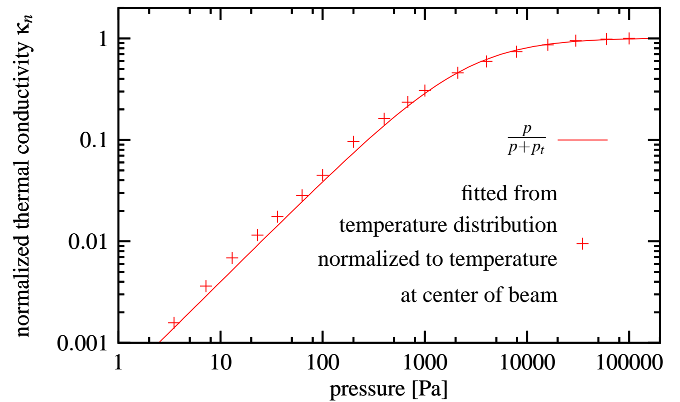

Figure 20. Normalized thermal conductivity versus pressure obtained from normalized temperature distribution for the fluid nitrogen.

product is fitted.

CONCLUSIONS

A Pirani pressure sensor with distributed temperature sensing above a v-grooved heat sink has been realized. Compared to a sensor which measures only the average temperature of the beam, the advantages are the increased working range and the independence of the Temperature Coefficient of Resistance of the sensors on the beam. The first advantage is due to the ability to take in account the heat transfer through the beam to its support, which extends the lower pressure range. The second advantage is due to the normalization of the temperature distribution to the temperature rise at the center, which cancels out the TCR.

The temperature measurements are not measured in a single point, but are averaged over each resistor segment. This has been taken in account in the used model to fit the measurement data. For pressures from 3.5 Pa up to 1 bar the thermal conductance to the bulk is extracted from the temperature distribution. A first order behaviour fits well through the thermal conductance-pressure plot.

ACKNOWLEDGMENT

The authors would like to thank Erwin Berenschot and Meint de Boer for their advice on the technological part and Remco Sanders for his advice on the measurement part. This research is supported by the Dutch technology foundation STW.

Copyright © 2001 by ASME

REFERENCES

[AJB95] W.J. Alvesteffer, D.C Jacobs, and D.H. Baker. Miniaturized thin film thermal vacuum sensor. *J. Vac. Sci. Technol.*, A 13(6):2980–2985, 1995.

[BK94] Ulrich Bonne and Dave Kubisiak. Burstproof, thermal pressure sensor for gases. *Solid-State Sensor and Actuator Workshop Hilton Head*, pages 78–81, 1994.

[Bru94] H.H. Bruun. *Hot-Wire Anemometry*. Oxford University Press, 1994.

[CCS99] Bruce C.S. Chou, Chung-Nan Chen, and Jin-Shown Shie. Micromachining on 111-oriented silicon. *Sensors and Actuators 75*, pages 271–277, 1999.

[Pau95] O. Paul. Vacuum gauging with complementary metal-oxide semiconductor microsensors. *J. Vac. Sci. Technol.*, A 13(3):503–508, 1995.

[Rei65] Frederick Reif. *Fundamentals of statistical and thermal physics*. McGraw-Hill, 1965.

[SN94] Nicholas R. Swart and Arokia Nathan. An integrated cmos polysilicon coil-based micro-pirani gauge with high heat transfer efficiency. *IEEE*, pages 135–138, 1994.

[VB96] Mattias Vangbo and Ylva Bäcklund. Terracing of (100) si with one mask and one etching step using misaligned v-grooves. *Journal of Micromechanics and Microengineering*, 6(1):39–41, 1996.

[vBWL+01] J.J. van Baar, R.J. Wiegerink, T.S.J. Lammerink, G.J.M. Krijnen, and M. Elwenspoek. Micromachined structures for thermal measurements of fluid and flow parameters. *JMM*, volume 11, issue 4 (July):311–318, 2001.

[vHS87] A.W. van Herwaarden and P.M. Sarro. Double-beam integrated thermal vacuum sensor. *J.Vac.Sci.Technol.*, A Vol. 5 No. 4:2454–2457, 1987.

[vP06] M. von Pirani. Selbszeigendes vakuum-mefsinstrument. *Verhandlungen der Deutschen Physikalischen Gesellschaft*, pages 686–694, 1906.

[vS11] M. von Smoluchowski. Zur theorie der warmteleitung in verdunnten gasen und der dabei auftretenden druckkrafte. *Annalen der Physik*, 35:983–1004, 1911.

[VS83] Jiri Vlach and Kishore Singhal. *Computer methods for circuit analysis and design*. van nostrand reinhold, 1983.

[WS94] Ping Kuo Weng and Jin-Shown Shie. Micro-pirani vacuum gauge. *Rev. Sci. Instrum. 65 (2)*, pages 492–499, 1994.

Copyright © 2001 by ASME